transitions is that allowing for orbital relaxation lowers the predicted excitation energies, generally by 0.3–0.5 eV. Thus transition-state excitation energies would probably be very close in absolute value to those observed experimentally. This additional evidence that the calculations are consistent with experiment further increases our confidence in our previously presented[2] conclusions about bonding in $Rh_2Cl_2(CO)_4$.

HF LCAO Calculations of $Rh_2Cl_2(CO)_4$. $Rh_2Cl_2(CO)_4$ has recently been treated theoretically by a nonempirical Hartree–Fock LCAO method, using a pseudopotential to represent the core orbitals.[7] Insofar as the discussion in this paper parallels our own work, there appears to be good agreement between the two calculations. In the folded conformation, a Mulliken population analysis of the LCAO orbitals yields charges of $Rh^{-0.11}$, $Cl^{-0.13}$, $C^{+0.38}$, and $O^{-0.26}$. We can obtain atomic charges from the $X\alpha$–SW orbitals by normalizing the total number of valence electrons found within the atomic spheres to the total number possessed by the molecule;[15] this gives $Rh^{-0.09}$, $Cl^{-0.15}$, $C^{+0.46}$, and $O^{-0.34}$. It is encouraging to see such close agreement between two very different methods of estimating charge.

The HF LCAO ordering for the mainly Rh 4d orbitals is identical with ours; there are minor differences in the ordering of the mainly Cl 3p orbitals. The other authors do not discuss the possibility of a weak Rh–Rh bonding interaction in the mainly Cl 3p orbitals, which we found to be the reason for the folding of the molecule. They do report a result which we did not, namely, that the folded form is calculated to be 4.1 kcal/mol more stable than the planar form. Given the close agreement between the two calculations in other respects, we would not be surprised if an analysis of the HF LCAO mainly Cl orbitals also revealed an enhanced Rh–Rh interaction upon folding.

(14) J. F. Nixon, R. J. Suffolk, and M. J. Taylor, paper in preparation.
(15) J. G. Norman Jr., *Inorg. Chem.*, **16**, 1028 (1977).

Experimental Section

$Rh_2Cl_2(CO)_4$ was prepared by the method of Wilkinson[16] by reaction of $RhCl_3 \cdot xH_2O$ with CO at ca. 90 °C. The sample was purified by vacuum sublimation at 80 °C (10^{-3} mmHg) and the IR spectrum checked prior to recording the He I and He II PE spectra. $Rh_2Cl_2(PF_3)_4$ was prepared from $Rh_2Cl_2(C_2H_4)_4$[17] by treatment with PF_3[18] and purified by sublimation at 20 °C (10^{-3} mmHg), and the ^{19}F NMR and IR spectra were checked prior to recording the PE spectrum.

He I photoelectron spectra were recorded on a PS16 Perkin-Elmer spectrometer. The $Rh_2Cl_2(PF_3)_4$ was vaporized into the instrument via an external inlet held at room temperature. $Rh_2Cl_2(CO)_4$ was vaporized internally at 60 ± 1 °C.

The spectra were recorded several times over a 6-h period and in all cases the reproducibility was excellent. No traces of free PF_3 or CO were observed under our conditions.

Acknowledgment. J.G.N., D.E.H., and D.J.G. thank the donors of the Petroleum Research Fund, administered by the American Chemical Society, and the National Science Foundation for support. J.G.N. is a Fellow of the Alfred P. Sloan Foundation for 1978–1980. J.F.N. thanks NATO for partial support of the work, and M.J.T. acknowledges the award of an SRC studentship. We thank Drs. J. C. Green and E. A. Seddon (Oxford University) for recording the He II spectrum and Professor M. F. Lappert for the use of the Sussex spectrometer.

Registry No. $Rh_2Cl_2(CO)_4$, 14523-22-9; $Rh_2Cl_2(PF_3)_4$, 14876-98-3.

(16) J. A. McCleverty and G. Wilkinson, *Inorg. Synth.*, **8**, 211 (1966).
(17) R. Cramer, *Inorg. Chem.*, **1**, 722 (1962).
(18) D. A. Clement and J. F. Nixon, *J. Chem. Soc., Dalton Trans.*, 2553 (1972).

Contribution from the Department of Chemistry,
State University of New York at Buffalo, Buffalo, New York 14214

Experimental Observation of the Effect of Crystal Field Splitting on the Electron Density Distribution of Iron Pyrite

E. D. STEVENS,* M. L. DELUCIA, and P. COPPENS*

Received June 5, 1979

The electron density distribution of iron pyrite, FeS_2, has been determined from high-resolution single-crystal X-ray diffraction measurements. Data collected with Ag Kα radiation to a resolution of $(\sin\theta)/\lambda = 1.46$ Å^{-1} were refined by conventional least-squares techniques to $R = 1.8\%$ and $R_w = 1.5\%$. Pyrite contains low-spin Fe^{2+} ions at $\bar{3}$ sites surrounded by a trigonally distorted octahedron of sulfur atoms. The crystal field splitting of the iron d orbitals is clearly revealed in the electron density maps by eight peaks of 1.2–1.6 e/Å^{-3} at 0.6 Å from the iron directed into the faces of the octahedron as expected for a $(t_{2g})^6(e_g)^0$ electronic configuration. The slight trigonal distortion further splits the t_{2g} orbitals into a_g and e_g orbitals. Refinement of the X-ray data including multipole parameters that describe the deformations from a spherical charge distribution yields occupancies of 2.0 (1) and 3.2 (2) e in the a_g and lower e_g orbitals and 0.8 (2) e in the upper e_g orbitals. The electric field gradient at the iron nucleus calculated from the multipole parameters due to the trigonal distortion explains the observed magnitude of the quadrupole splitting in the Mössbauer spectra. The results are discussed in view of the observed diamagnetism of pyrite.

Introduction

In the presence of strong crystal fields, electrons in the partially filled d shell of a transition metal will preferentially occupy the lower energy orbitals, resulting in an aspherical distribution of the electron density about the metal atom. In recent years, techniques for the experimental determination of electron density distributions in crystals have been developed by using accurate X-ray (and neutron) diffraction measurements.[1] While the number of experimental electron density studies on systems containing transition metals is still rather limited, several investigations have found aspherical features clearly related to partial occupancy of the d orbitals.[2] More

(1) (a) P. Coppens and E. D. Stevens, *Adv. Quantum Chem.*, **10**, 1 (1977); (b) P. Coppens, *MTP Int. Rev. Sci.: Phys. Chem., Ser. Two*, **11**, 21 (1975).

0020-1669/80/1319-0813$01.00/0

Table I. Crystallographic Data for Iron Pyrite and Experimental Conditions

$a = 5.4160(2)$ Å	space group: $Pa\bar{3}$
$Z = 4$	Fe at (0, 0, 0): $\bar{3}$
$D_x = 5.016$ g cm^{-3}	S at (x, x, x): 3

radiation: Ag Kα ($\bar{\lambda} = 0.560\ 87$ Å)
μ(Ag Kα) = 58.0 cm^{-1}
β filter: 0.025-mm Pd foil
$T = 21$ °C
takeoff angle = 3.0°
receiving aperture: 6.0 × 6.0 mm at 22 cm from crystal

quantitative estimates of the d-orbital occupancies have been obtained in recent studies of the octahedral complexes $Cr(CO)_6$[3] and $[Co(NH_3)_6][Cr(CN)_6]$.[4]

To assess the reliability of experimental charge density measurements on transition metals and explore the extent to which quantitative information on the electronic structure can be obtained, we have determined the electron density distribution in pyrite (FeS_2) from high-resolution X-ray intensity measurements. Cubic pyrite contains iron formally in the ferrous (2+) state and discrete disulfide (S_2^{2-}) ions. The nearest-neighbor sulfur atoms form a trigonally distorted octahedron about the iron. Magnetic susceptibility[5] and Mössbauer spectroscopy[6] measurements indicate a low-spin state for the iron, suggesting population of the t_{2g} orbitals by all six d electrons. The iron is therefore expected to show a large asphericity in its density distribution. The low thermal motion of the mineral pyrite makes it well suited for a detailed high-resolution analysis.

Experimental Section

Data Collection. Small crystals from a sample of natural pyrite (Zacatecas, Mexico) were ground into spheres. Those crystals that appeared most nearly spherical were mounted on a diffractometer and intensities of several symmetry-related reflections measured. After examination of several crystals, a sphere of 0.09-mm diameter was found to give satisfactory agreement between symmetry-equivalent reflections and was selected for data collection.

The setting angles of 30 reflections in the range $70° < 2\theta < 90°$ were carefully measured and used in a least-squares refinement of the unit-cell dimensions and crystal orientation. Some samples of pyrite are reported to be noncubic.[7] Independent refinement of the six cell dimensions and angles indicated the unit cell to be cubic within the estimated standard deviations. Crystallographic information is summarized in Table I.

Intensity measurements were collected at room temperature on a Picker FACS-I automated diffractometer using Pd-filtered Ag Kα radiation and a θ–2θ step–scan technique. Each reflection was scanned from $2\theta(K\alpha_1) - 1.1°$ to $2\theta(K\alpha_2) + 1.1°$ with a step size of 0.02° in 2θ and a count time of 2 s/step. The full step–scan profile of each reflection was recorded on magnetic tape and analyzed to give integrated intensities and estimated standard deviations.[8]

A standard reflection measured after every 30 reflections and 9 additional standards measured after every 90 reflections showed no significant change in intensity during data collection. A total of 9200 reflections were collected in the range $0° < 2\theta < 110°$, corresponding to approximately 12 symmetry-related measurements of each independent reflection. Absorption corrections for a sphere of 0.09-mm diameter were obtained by interpolation from calculated tables.[9] Averaging symmetry-related reflections gave 705 independent reflections and an internal agreement factor $R(F^2) = 2.6\%$ (1.3% for the 2500 measurements with $F^2 > 100\sigma(F^2)$). The excellent agreement between symmetry-related reflections further confirms the cubic space group.

Least-Squares Refinements. The quantity $\sum w(F_o - k|F_c|)^2$ with $w = 1/(\sigma^2(F))$ was minimized by full-matrix least-sqaures refinement including adjustment of an isotropic secondary extinction parameter.[10] In each refinement, the best fit to the observed intensities was obtained from a type I extinction model with a Lorentzian mosaic distribution. Inclusion of a primary extinction parameter[10] did not significantly improve the fit. The estimated standard deviation of each observation $\sigma(F^2)$ was taken as the larger of σ_1 and σ_2, where $\sigma_1^2 = \sigma^2_{count} + (0.01F^2)^2$ and $\sigma_2^2 = \sum^n(F_i^2 - \langle F^2\rangle)^2/(n-1)$ for n symmetry-related observations. Reflections with both F_o and F_c less than $\sigma(F)$ were considered "unobserved" and were not included in the refinement. Atomic scattering factors for Fe and S and core and valence scattering factors for S were taken from ref 11a. Core scattering factors for Fe were calculated by subtracting 4s[11b] and 3d[11a] scattering factors from the total atomic scattering factors. Anomalous scattering factors for both Fe and S from ref 12 were included in the calculations.

To allow for possible deviations from harmonic thermal motion, we used an expansion of the temperature factor to include third and fourth cumulant parameters[13] in the least-squares model for some refinements. The temperature factor is modified by the expression

$$\exp\left[-i\frac{4\pi^3}{3}\sum C_{ijk}h_ih_jh_ka_i^*a_j^*a_k^* + \frac{2\pi^4}{3}\sum D_{ijkl}h_ih_jh_kh_la_i^*a_j^*a_k^*a_l^*\right]$$

where the C_{ijk} and D_{ijkl} are the third and fourth cumulant parameters in addition to the conventional harmonic parameters U_{ij} to be varied in the refinement.

Since refined positional and thermal parameters will be biased by the aspherical features of the valence density,[14] several refinements have been made with only high-order reflections, the intensity of which is largely due to the core electrons.[15]

To test for possible deviations from ideal stoichiometry, we allowed the occupancy of the sulfur site to vary together with other parameters in an initial refinement. Only data with $(\sin\theta)/\lambda > 0.85$ Å^{-1} were refined to avoid bias from the valence density. Refinement yielded a stoichiometry of $FeS_{1.994(13)}$, which has judged sufficiently close to the ideal value. In all further refinements the ideal stoichiometry was used.

In order to obtain quantitative information on the extent of the distortion of the d-shell density on iron, further refinements have been made including density functions describing the distortion.[16] For iron, the atomic density is represented by eq 1, where ρ_{core} and ρ_{4s}

$$\rho_{Fe}(\mathbf{r}) = \rho_{core}(\mathbf{r}) + \sum_{lm} P_{lm}(R_l(r))y_{lm}(\mathbf{r}/r) + P_{4s}\rho_{4s}(\mathbf{r}) \quad (1)$$

are the spherical Hartree–Fock core and 4s densities for iron, y_{lm} is the spherical harmonic angular functions in real form, and P_{lm} and ρ_{4s} are the adjustable population parameters. The radial functions $R_l(r)$ are given by eq 2, where N is a normalization factor[16] and ζ

$$R_l(r) = N^{-1}r^{n_l}e^{-2\zeta r} \quad (2)$$

is an adjustable parameter. For iron, n_l is taken to be equal to 4, which represents the radial dependence of the product of Slater 3d functions.

(2) (a) M. Iwata and Y. Saito, *Acta Crystallogr., Sect. B*, **29**, 822 (1973); (b) B. Rees and P. Coppens, *ibid.*, **29**, 2516 (1973); (c) H. Miyamae, S. Sato, and Y. Saito, *ibid.*, **33**, 3391 (1977); (d) C. L. Davis, E. N. Maslen, and J. N. Varghese, *Acta Crystallogr., Sect. A*, **34**, 371 (1978); (e) Y. Wang and P. Coppens, *Inorg. Chem.*, **15**, 1122 (1976).
(3) B. Rees and A. Mitschler, *J. Am. Chem. Soc.*, **98**, 7918–24 (1976).
(4) M. Iwata, *Acta Crystallogr., Sect. B*, **33**, 59 (1977).
(5) L. A. Marusak, C. Cordero-Montalvo, and L. N. Mulay, *Mater. Res. Bull.*, **12**, 1009 (1977).
(6) S. L. Finklea, L. Cathey, and E. L. Amma, *Acta Crystallogr., Sect. A*, **32**, 529 (1976).
(7) P. Bayliss, *Am. Mineral.*, **62**, 1168 (1977).
(8) R. H. Blessing, P. Coppens, and P. Becker, *J. Appl. Crystallogr.*, **7**, 488 (1974).
(9) C. W. Dwiggins, *Acta Crystallogr., Sect. A*, **31**, 395 (1975).
(10) (a) P. J. Becker and P. Coppens, *Acta Crystallogr., Sect. A*, **30**, 129 (1974); (b) P. J. Becker and P. Coppens, *ibid.*, **30**, 148 (1974).
(11) (a) "International Tables for X-Ray Crystallography", Vol. IV, Kynoch Press, Birmingham, England, 1974; (b) D. T. Cromer, private communication.
(12) D. T. Cromer and D. Liberman, *J. Chem. Phys.*, **53**, 1891 (1970).
(13) C. K. Johnson, *Acta Crystallogr., Sect. A*, **25**, 187 (1969).
(14) P. Coppens, *Acta Crystallogr., Sect. B*, **30**, 255 (1974).
(15) E. D. Stevens and H. Hope, *Acta Crystallogr., Sect. A*, **31**, 494 (1975).
(16) N. K. Hansen and P. Coppens, *Acta Crystallogr., Sect. A*, **34**, 909 (1978).

Table II. Spherical Atom Refinements[a]

	refinement		
	I	II	III
(sin θ)/λ range, Å^{-1}	0.0–1.46	0.85–1.46	0.85–1.46
N_{obsd}	578	442	443
N_v	7	7	21
discrep indices R,[b] %	1.84	2.26	2.12
discrep indices R_w,[c] %	1.47	1.49	1.32
discrep indices including unobsd reflctns R, %	3.72	5.26	5.13
discrep indices including unobsd reflctns R_w, %	1.54	1.62	1.46
discrep indices including unobsd reflctns GOF[d]	1.51	1.28	1.14
scale factor (k)	4.017 (7)	4.020 (13)	4.101 (38)
Fe U_{11} (Å^2)	0.002 63 (5)	0.002 60 (3)	0.002 94 (18)
Fe U_{12}	−0.000 04 (4)	0.000 05 (1)	−0.000 17 (5)
S x	0.384 85 (5)	0.384 82 (2)	0.384 86 (6)
S U_{11}	0.003 20 (7)	0.003 19 (3)	0.003 71 (20)
S U_{12}	0.000 03 (6)	0.000 05 (2)	0.000 02 (7)
extinction (g)	1.04 (3) × 10^{-4}	1.34 (15) × 10^{-4}	1.45 (15) × 10^{-4}

	refinement		
	IV	V	VI
(sin θ)/λ range, Å^{-1}	0.0–1.46	0.0–1.46	0.0–1.46
N_{obsd}	577	577	578
N_v	21	35	37
discrep indices R, %	2.05	1.82	1.78
discrep indices R_w, %	1.62	1.34	1.30
discrep indices including unobsd reflctns R, %	3.91	3.70	3.67
discrep indices including unobsd reflctns R_w, %	1.68	1.42	1.38
discrep indices including unobsd reflctns GOF[d]	1.68	1.42	1.37
scale factor (k)	4.123 (9)	4.125 (14)	4.038 (16)
Fe U_{11}	0.002 66 (2)	0.002 34 (8)	0.002 19 (8)
Fe U_{12}	−0.000 04 (2)	−0.000 22 (8)	−0.000 20 (10)
S x	0.384 84 (2)	0.384 88 (3)	0.384 87 (3)
S U_{11}	0.003 54 (3)	0.003 99 (10)	0.003 64 (11)
S U_{12}	0.000 07 (2)	0.000 07 (5)	0.000 10 (5)
extinction (g)	1.44 (4) × 10^{-4}	1.38 (4) × 10^{-4}	1.07 (4) × 10^{-4}

[a] Refinement: I, conventional refinement of full data set; II, high-order refinement; III, high-order refinement including third and fourth cumulant parameters; IV, full data refinement including multipole parameters; V, full data multipole refinement including third and fourth cumulants; VI, same as V but including refinement of total d-electron population on iron. [b] $R = \Sigma ||F_o| - |F_c|| / \Sigma |F_o|$. [c] $R_w = [\Sigma w(|F_o| - |F_c|)^2 / \Sigma w|F_o|^2]^{1/2}$. [d] GOF $= [\Sigma w(|F_o| - |F_c|)^2 / (N_{obsd} - N_v)]^{1/2}$.

P_{lm}, P_{4s}, and ζ are refineable parameters. For sulfur, the atomic density is given by eq 3, where ρ_{core} and ρ_{val} are spherical Hartree–Fock core

$$\rho_S(\mathbf{r}) = \rho_{core}(\mathbf{r}) + P_{val}\rho_{val}(\kappa\mathbf{r}) + \sum P_{lm}(R_l(\kappa\mathbf{r}))y_{lm}(\mathbf{r}/r) \quad (3)$$

and valence densities for sulfur and P_{val}, P_{lm}, and κ are adjustable parameters. In all refinements, populations have been constrained to maintain electroneutrality in the crystal.

Electron Density Maps. The experimental electron density distribution is displayed in plots of the deformation density, $\Delta\rho$, defined as the difference between the total observed density and the density calculated from a superposition of spherical, neutral Hartree–Fock atoms

$$\Delta\rho = \rho(\text{obsd})/k - \rho(\text{spherical atoms}) = \frac{1}{V}\sum(F_o/k - F_c)e^{2\pi i\mathbf{S}\cdot\mathbf{r}} \quad (4)$$

where k is the X-ray scale factor. Positions and thermal parameters used in calculating ρ(spherical atoms) were taken from the high-order refinements. The deformation maps were calculated with the use of the full X-ray data to a resolution of (sin θ)/λ = 1.2 Å^{-1} corrected for extinction and anomalous dispersion. The scale factor was obtained by a cycle of refinement on k with all other parameters fixed at the high-order values.

The deformation density corresponding to the model fitted by the multipole refinement is calculated by subtracting spherical-atom structure factors from structure factors calculated from the deformation parameters:

$$\Delta\rho(\text{model}) = \frac{1}{V}\sum(F_c(\text{model}) - F_c(\text{spherical atoms}))e^{2\pi i\mathbf{S}\cdot\mathbf{r}} = \rho(\text{model}) - \rho(\text{spherical atoms}) \quad (5)$$

In this definition, the model deformation density includes smearing due to thermal motion of the atoms and is series terminated at the same resolution as the experimental data.

The residual density given by the difference between the observed density and the density corresponding to the multipole model

$$\Delta\rho(\text{residual}) = \rho(\text{obsd})/k - \rho(\text{model}) \quad (6)$$

is a useful function for analyzing the success of the multipole model in fitting the significant features. Ideally, the residual density should only show fluctuations that are not significant as judged by the estimated error distribution.

Error Maps. The distribution of errors in the experimental deformation density contains contributions from the errors in the structure factors, errors in the refined positional and thermal parameters, and error in the scale factor. The first contribution is relatively constant, except near crystallographic symmetry elements, while the other two increase rapidly near the atomic centers, making the experimental density distribution unreliable near the nuclear positions. The contributions to $\sigma(\Delta\rho)$ have been calculated as described previously.[17]

Results

Spherical-Atom Refinements. Conventional least-squares refinement on the full X-ray data set starting with the parameters of Finklea, Cathey, and Amma[6] converged to R = 1.84% and R_w = 1.47%. The results of the refinement are tabulated in Table II (refinement I). Each iron is surrounded by six sulfur atoms at 2.2633 (2) Å, forming a trigonally distorted octahedron. The S–Fe–S angles are 94.355 (4) and 85.645 (2)°. The nearest-neighbor sulfur atoms are covalently bonded to six next-nearest-neighbor sulfurs with an S–S distance of 2.1604 (3) Å. These values do not significantly differ

(17) (a) E. D. Stevens, *Acta Crystallogr., Sect. B*, **34**, 544 (1978); (b) B. Rees, *Acta Crystallogr., Sect. A*, **32**, 483 (1976).

Table III. Third and Fourth Cumulant Thermal Parameters ($\times 10^6$) (Å^3 and Å^4, Respectively)

		refinement		
		III	V	VI
Fe	D_{1111}	5 (5)	−18 (3)	−16 (3)
	D_{1112}	−12 (2)	−5 (3)	−3 (3)
	D_{1222}	2 (2)	−4 (3)	−5 (3)
	D_{1122}	4 (2)	−7 (1)	−7 (1)
	D_{1123}	1 (1)	−2 (1)	−3 (1)
S	C_{111}	9 (12)	10 (9)	10 (9)
	C_{112}	0 (5)	1 (5)	0 (5)
	C_{122}	1 (5)	3 (5)	2 (5)
	C_{123}	−6 (7)	−7 (8)	−7 (8)
	D_{1111}	19 (6)	30 (5)	25 (5)
	D_{1112}	−3 (2)	−1 (2)	0 (2)
	D_{1222}	0 (2)	1 (2)	2 (2)
	D_{1122}	6 (2)	10 (2)	8 (2)
	D_{1123}	1 (1)	1 (1)	1 (1)

from previous results,[6] although the estimated standard deviations reported here are an order of magnitude lower. While the unusually low standard deviations reflect the higher resolution and internal consistency of the data, systematic effects such as the inadequacy of the least-squares model may introduce errors that are not reflected in the estimated standard deviations.

The results of least-squares refinement on the high-order X-ray data ($(\sin\theta)/\lambda > 0.85$ Å^{-1}) are given in Table II (refinement II). Although the R factors are slightly higher, the "goodness of fit" parameter is lower, indicating that the X-ray scattering at high angles more closely corresponds to the spherical-atom model used in the refinement. The bond distances and angles derived from the high-order parameters do not differ significantly from those of the full data refinement.

In most previous charge density studies of light-atom structures, possible deviations of the atomic thermal motion from the harmonic model have been ignored. For studies at high resolution and for structures containing heavier elements, however, small deficiencies in the model may produce significant errors in the derived density.[18] Refinement using a cumulant expansion of the temperature factor introduces additional parameters that describe the deviations of the thermal smearing function from a normal probability distribution. The results of refinement with third and fourth cumulant parameters (as allowed by symmetry) are given in Tables II and IV (refinement III). Since the higher cumulant parameters may also be biased by valence features,[19] they have been determined by refinement of the high-order data. The improvement in the model is found to be highly significant at the 0.5% confidence level, as judged by Hamilton's R-factor ratio test.[20]

Aspherical-Atom Refinements. The results of least-squares refinement with multipole density functions describing the atomic deformations included as parameters are given in Tables III and IV (refinements IV–VI). Additional third and fourth cumulant parameters included in refinements V and VI are again significant as judged by the R-factor ratio test.

If we assume that the d orbitals on the iron can be represented by single Slater-type orbitals and that the overlap between metal and ligand orbitals can be neglected (the crystal field approximation), then there is a linear relationship between the multipole density parameters and the populations of the iron d orbitals.[21] In an octahedral field, the d orbitals are split into t_{2g} and e_g orbitals. In a trigonally distorted field, the t_{2g} orbitals are further split into a_g and e_g orbitals (Figure 1). The distribution of the iron d electrons will be given by a sum over the squares of the atomic orbitals as in eq 7, where

$$\rho(\mathbf{r}) = [R(r)]^2\left[P_1 y_{a_g}^2 + \frac{1}{2}P_2\left(y_{e_{g+}}^2 + y_{e_{g-}}^2\right) + \frac{1}{2}P_3\left(y_{e_{g+}'}^2 + y_{e_{g-}'}^2\right) + P_4(y_{e_{g+}} + y_{e_{g-}})(y_{e_{g+}'} + y_{e_{g-}'})\right] \quad (7)$$

$R(r)$ is the radial part, y_{a_g}, $y_{e_{g+}}$, ... are angular functions formed by symmetry-adapted combinations of Slater d functions,[4] and P_1, P_2, and P_3 are the populations (number of electrons) in the a_g, e_g, and e_g' orbitals. An additional cross term is present because the lower and upper e_g orbitals belong to the same symmetry representation. The additional parameter P_4 is related to the extent of mixing.

Taking the products of second-order spherical harmonics (d functions) yields a linear combination of spherical harmonics of order 4, 2, and 0. These functions have the same angular dependence as the allowed multipole density functions at a $\bar{3}m$

Table IV. Multipole Density Functions[a]

		refinement		
		IV	V	VI
Fe	ζ_{3d}, au^{-1}	3.91 (3)	3.76 (3)	4.15 (5)
	P_{4s}	0.0	0.0	0.0
	P_{00}	6.0	6.0	4.44 (15)
	P_{20}	−0.01 (3)	0.07 (4)	0.05 (4)
	P_{40}	0.21 (3)	0.23 (3)	0.25 (4)
	P_{43+}	−0.29 (3)	−0.28 (3)	−0.29 (3)
	P_{43-}	0.00 (3)	−0.01 (3)	−0.01 (3)
S	ζ_{val}	4.07 (4)	3.86 (4)	3.48 (4)
	P_{val}	7.0	7.0	7.78 (7)
	P_{10}	0.22 (5)	0.23 (5)	0.58 (7)
	P_{20}	−0.21 (5)	−0.24 (5)	−0.52 (6)
	P_{30}	−0.01 (4)	0.01 (4)	−0.05 (6)
	P_{33+}	0.11 (3)	0.12 (3)	0.20 (4)
	P_{33-}	0.02 (3)	0.03 (3)	0.02 (3)
	P_{40}	0.00 (4)	−0.02 (4)	0.04 (5)
	P_{43+}	0.13 (4)	0.13 (4)	0.18 (5)
	P_{43-}	0.02 (3)	0.03 (3)	0.02 (3)

[a] Local coordinate systems for multipole functions: for iron, z axis along threefold axis, x axis such that nearest sulfur atom lies in xz plane; for sulfur, z axis along threefold axis directed toward the center of the S–S bond, x axis is such that the iron atom lies in xz plane.

Table V. Iron Orbital Occupancies and Electric Field Gradients

	refinement		
	IV	V	VI
P_1	1.77 (10)	2.00 (13)	1.67 (14)
P_2	3.41 (13)	3.24 (16)	2.69 (19)
P_3	0.82 (13)	0.76 (15)	0.08 (17)
P_4	0.11 (19)	−0.11 (26)	0.01 (29)
V_{zz}, 10^{-14} esu^{-1} cm^3	2 (8)	−17 (10)	−16 (14)

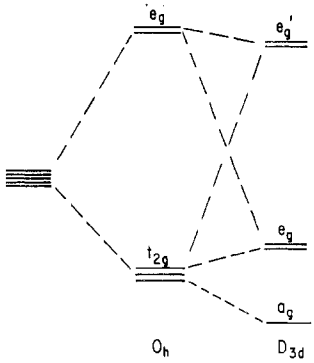

Figure 1. Energy level diagram showing the splitting of d orbitals by an octahedral electrostatic crystal field and the further splitting of the t_{2g} orbitals by a trigonal distortion.

(18) E. D. Stevens, *Mol. Phys.*, **37**, 27 (1979).
(19) E. D. Stevens and H. Hope, *Acta Crystallogr., Sect. A*, **33**, 723 (1977).
(20) W. C. Hamilton, *Acta Crystallogr.*, **18**, 502 (1965).
(21) E. D. Stevens and P. Coppens, *Acta Crystallogr., Sect. A*, **35**, 536 (1979).

(D_{3d}) site. The relation between the multipole population parameters P_{00}, P_{20}, P_{40}, and P_{43+} and the d-orbital occupancies P_1, P_2, P_3, and P_4 are given by eq 8,[21] where the constants C_{lm}

$$P_{00} = (P_1 + P_2 + P_3)\left(\frac{1}{4\pi}\right)^{1/2} C_{00}$$

$$P_{20} = (2P_1 - P_2 - 2^{1/2}P_4)\left(\frac{5}{196\pi}\right)^{1/2} C_{20}$$

$$P_{40} = \left(6P_1 - \frac{2}{3}P_2 - \frac{7}{3}P_3 + \frac{5(2^{1/2})}{3}P_4\right)\left(\frac{1}{196\pi}\right)^{1/2} C_{40}$$

$$P_{43+} = \left(P_3 - P_2 + \frac{1}{3}P_4\right)\left(\frac{5}{56\pi}\right)^{1/2} C_{43} \qquad (8)$$

$= N_{lm}$(wave function)/N_{lm}(density function) occur because of a difference in normalization of wave functions and density functions.[16]

These four equations may be solved for the four unknown d-orbital occupancies P_1, P_2, P_3, and P_4, to give the results listed in Table V. Estimated standard deviations include the effect of correlations between the least-squares parameters.

In this analysis, only the nearest-neighbor sulfur atoms have been considered, giving an effective crystal field with $\bar{3}m$ (D_{3d}) symmetry at the iron site. The y_{43+} multipole density function is defined with positive lobes directed toward the sulfur atoms. A larger occupancy of the e_g than of the e_g' orbitals ($P_2 > P_3$) will normally result in a negative P_{43+} parameter. The true site symmetry for the iron, however, is $\bar{3}$ (S_6), and an additional multipole function y_{43-} is allowed. No further splitting of the d orbitals occurs in the lower symmetry field, but the orientation of the effective crystal field may be rotated about the threefold axis. However, the population of the y_{43-} multipole is found to be insignificant, confirming the validity of treating the local crystal field as D_{3d}.

Refinements including the population of the iron 4s density as a variable yield unreasonably large negative charges on the iron atom. The 4s population cannot be reliably determined from the X-ray experiment since X-ray scattering from the diffuse density corresponding to the 4s orbital contributes significantly to only a few low-angle reflections that are also highly affected by extinction. Therefore, for refinements IV–VI the population of the 4s density function has been fixed at zero.

A further difficulty was encountered with the multipole parameters centered on sulfur. With use of the multipole model which has proved the most successful for light-atom structures and which allows separate radial dependences for the spherical and higher order terms,[16] the higher multipoles became more diffuse during refinement in an attempt to fit the density near the iron site. This behavior was corrected by restricting the spherical and higher multipoles to share a common radial parameter κ and fixing n_l equal to 4 for all values of l in the radial function (eq 2).

In refinements IV and V the total number of electrons in the iron d shell has been fixed at 6. Refinement with fixed monopole populations as in IV but no higher multipole parameters gives $R = 2.26\%$, $R_w = 1.94\%$, and GOF = 1.99. The higher agreement factors for refinement IV compared to those for refinement I may therefore be attributed to the use of idealized atomic charges and the single Slater radial function used for the iron 3d electrons. Including the number of d electrons as a variable (refinement VI) produces a small but significant improvement of the model fit to the X-ray data. However, this refinement is less satisfactory than refinement V, especially with regard to the large negative charge (3.6–) on the disulfide ion.

Electric Field Gradient. From an experimental determination of the electron density distribution, other one-electron properties of the system can be calculated, either by direct integration of the charge density or from the populations of the refined multipole functions.[22] In iron pyrite, a property of particular interest is the electric field gradient (EFG) at the iron nucleus.[6] A nonzero EFG produces a quadrupole splitting of the Mössbauer spectra, which for an iron atom is given by eq 9,[23] where $eq = V_{zz}$ = principal component of the

$$\Delta E_{QS} = \frac{1}{2}e^2qQ(1 + \eta^{2/3})^{1/2} \qquad (9)$$

EFG tensor, Q = nuclear quadrupole moment, and η = asymmetry parameter. One can split q into contributions from the valence electrons on iron and from the charges in the surrounding lattice

$$q = (1 - \gamma_\infty)q_{lat} + (1 - R)q_{val} \qquad (10)$$

where γ_∞ and R are Sternheimer antishielding factors.[24]

For an octahedral $(t_{2g})^6$ electronic configuration, $q_{val} = 0$ and no contribution to the quadrupole splitting is expected from the d electrons. However, Finklea et al.[6] have shown that the calculated contributions from q_{lat} and deviations from ideal stoichiometry are too small to account for the magnitude of the observed splitting in pyrite. Therefore, we neglect these contributions and consider only q_{val} for the distorted complex.

The components of the EFG tensor are obtained by integration of the electron density distribution

$$V_{ij} = \int (\rho(\mathbf{r}))\hat{V}_{ij}\, d\mathbf{r} \qquad (11)$$

with the potential operator

$$\hat{V}_{ij} = -(3\mathbf{r}_i\mathbf{r}_j - r^2\delta_{ij})/r^5 \qquad (12)$$

If the $\rho(\mathbf{r})$ is expressed as a multipole expansion using spherical harmonic angular functions, only populations of the quadrupolar terms (y_{2m}) contribute.[25] For the density model given in eq 1 and 2, integration over the radial part gives

$$V_r = \int_0^\infty R(r)/r\, dr = (2\zeta)^3/[n_l(n_l + 1)(n_l + 2)] \qquad (13)$$

Direct evaluation of (11) yields the components of the electric field gradient in terms of the multipole populations P_{lm}:[26]

$$V_{11} = (3/5)V_r(\pi P_{22+} - 3^{1/2}P_{20})$$

$$V_{22} = (3/5)V_r(\pi P_{22+} + 3^{1/2}P_{20})$$

$$V_{33} = -(6/5)V_r(3^{1/2}P_{20})$$

$$V_{12} = -(3/5)V_r(\pi P_{22-})$$

$$V_{13} = -(4/5)V_r(\pi P_{21+})$$

$$V_{23} = -(4/5)V_r(\pi P_{21-}) \qquad (14)$$

Solving the cubic secular equation with the elements of the EFG tensor yields the principal components V_{xx}, V_{yy}, V_{zz}, which are labeled by convention such that $|V_{zz}| \geq |V_{yy}| \geq |V_{xx}|$. The asymmetry parameter is given by $\eta = (V_{xx} - V_{yy})/V_{zz}$ and may take values in the range 0–1.

In the case of FeS_2, it is evident from eq 8 that unequal populations of the a_g and e_g orbitals ($P_2 \neq 2P_1$) resulting from the trigonal distortion will result in a nonzero population of the y_{20} quadrupole splitting. The principal component of the EFG at the iron nucleus is given in Table V on the basis of the values of ζ and P_{20} from each of the multipole refinements. Note that for refinements V and VI the field gradient is

(22) (a) P. Coppens and W. C. Hamilton, *Acta Crystallogr., Sect. B*, **24**, 925 (1968); (b) P. Coppens, *Phys. Rev. Lett.*, **35**, 98 (1975); (c) P. Coppens and T. N. Guru Row, *Ann. N.Y. Acad. Sci.*, **313**, 244 (1978).
(23) G. M. Bancroft, "Mössbauer Spectroscopy: An Introduction for Chemists and Geochemists", McGraw-Hill, London, 1973.
(24) R. Sternheimer and H. M. Foley, *Phys. Rev.*, **102**, 731 (1956).
(25) R. F. Stewart, *J. Chem. Phys.*, **57**, 1664 (1972).
(26) These expressions differ from those in ref 25 because of differences in the definition and normalization of the density functions.

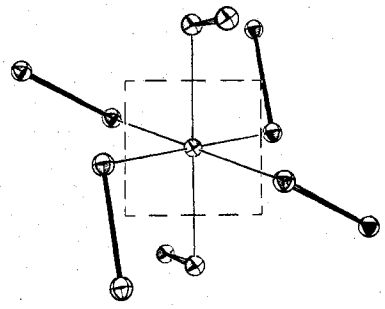

Figure 2. Coordination geometry of disulfide ions about iron in pyrite. Ellipsoids are plotted at 90% probability. The dashed lines define the section of the electron density distribution plotted in Figures 3 and 5. The plane contains the line connecting the iron atom with the nearest-neighbor axial sulfur atoms and bisects the angle between two of the equatorial sulfur atoms.

negative, in agreement with the experimentally determined sign.[27] Since y_{20} is the only allowed quadrupolar density function, $\eta = 0$. With $V_{zz} = -1.7 \times 10^{15}$ esu/cm^3 from refinement V and $Q_{Fe} = 0.2 \times 10^{-24}$ cm^2, $R = 0.22$,[6] and the conversion factor (for Fe) 1 erg = 0.13×10^{20} mm/s, the predicted contribution of q_{val} to the Mössbauer splitting is 0.8 (5) mm/s compared with the observed splitting of 0.634 (6) mm/s at room temperature.[6] Although the electric field gradient is not accurately determined by this X-ray experiment, it has the proper sign and order of magnitude to explain the origin of the observed quadrupole splitting.

Electron Density Maps. Preferential population of the t_{2g} orbitals of a metal atom in a strong octahedral field results in an aspherical density distribution with maxima pointing into the eight faces of the octahedron and minima directed toward the six ligands. With a trigonally distorted field, a difference in population of the a_g and lower e_g orbitals will result in a difference in peak heights between the two maxima along the threefold axis and the remaining six maxima distributed about the threefold axis. The plane defined in Figure 2 contains the two maxima along the threefold axis, two of the other six (equivalent) maxima, and the minima directed toward the two ligands in the plane.

In Figure 3, the experimental electron density distribution around the iron atom is mapped in the plane defined in Figure 2. This section reveals four peaks about the iron as expected for a low-spin configuration of the d electrons. Two peaks along the threefold axis (1.6 (3) e/Å^3) are higher than the other two (1.2 (2) e/Å^3), indicating a preference for population of the a_g over the e_g orbitals. This preference is in the direction expected from the threefold distortion that opens the angle between ligands about the a_g direction to 94.4° compared with the octahedral angle of 90°.

The distribution of the estimated standard deviation in the deformation density is plotted in Figure 3b. The standard deviation in the deformation density at a general position is estimated to be 0.20 e/Å^3 but increases near special symmetry positions. Along the threefold axis the estimated error increases to 0.34 e/Å^3. Within 0.25 Å of the iron site the error increases rapidly to 17.9 e/Å^3 at the nucleus, due to contributions from the errors in the thermal parameters and scale factor. Thus features of the electron density close to the iron nucleus are not reliably determined by the X-ray experiment.

The electron density distribution in the S_2^{2-} molecule is plotted in Figure 4a. The corresponding distribution of the estimated standard deviation is plotted in Figure 4b. A peak of 0.4 (3) e/Å^3 is located at 0.55 Å from each sulfur position along the S–S bond. Though these features are similar to the

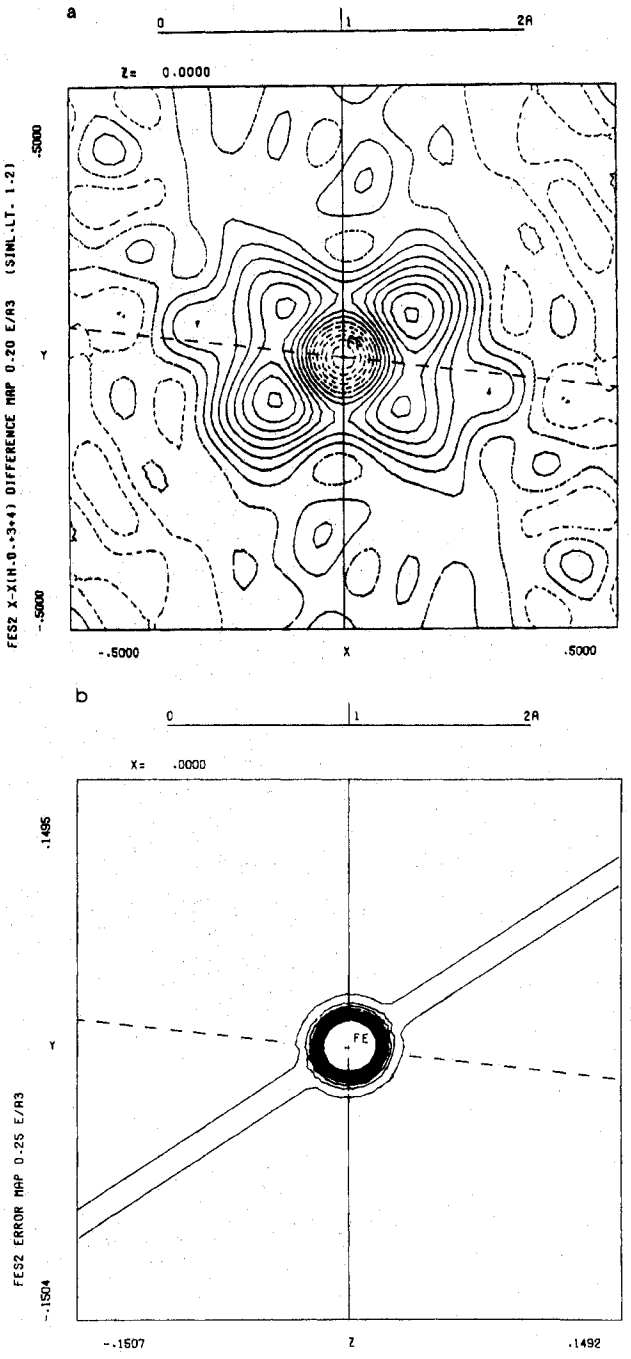

Figure 3. (a) Experimental deformation density about the iron atom in FeS_2 calculated by using X-ray structure factors to a resolution of $(\sin\theta)/\lambda = 1.2$ Å^{-1}. Contours are plotted at 0.2 e/Å^3 intervals with the zero and negative contours broken. (b) Estimated error distribution of the deformation density in the same plane as Figure 3a. Contours are plotted at 0.25 e/Å^3 intervals starting at 0.25 e/Å^3. Contours above 5 e/Å^3 have been omitted.

electron density distribution in the bonds of the S_8 molecule[28] and the isoelectronic Cl_2 molecule,[18] they are not sufficiently larger than the estimated errors to allow further interpretation.

In Figure 5a, the model deformation density about the iron atom is plotted as calculated from the deformation parameters of refinement V. This map is calculated by including all terms in the Fourier series to the limit of the experimental resolution (1.46 Å^{-1}) and includes the effects of smearing by the thermal motion of the iron atom. The residual density in the same

(27) P. A. Montano and M. S. Seehra, *Solid State Commun.*, **20**, 897 (1976).

(28) P. Coppens, Y. W. Yang, R. H. Blessing, W. F. Cooper, and F. K. Larsen, *J. Am. Chem. Soc.*, **99**, 760 (1977).

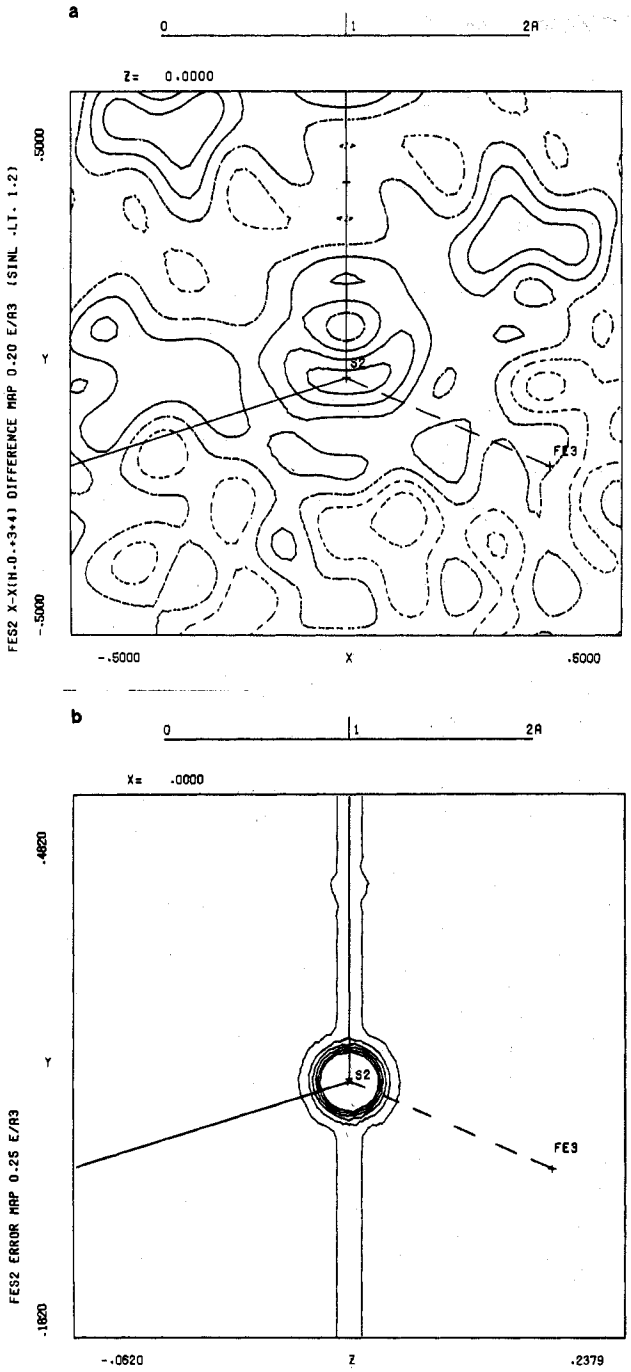

Figure 4. (a) Experimental deformation density in the S–S bond. The section plotted is centered at a sulfur atom with the bond axis along the vertical direction and one of the three nearest iron atoms in the plane. Contours are plotted as in Figure 3a. (b) Estimated error distribution of the deformation density in Figure 4a. Contours are plotted as in Figure 3b with contours above 1.5 e/Å^3 omitted.

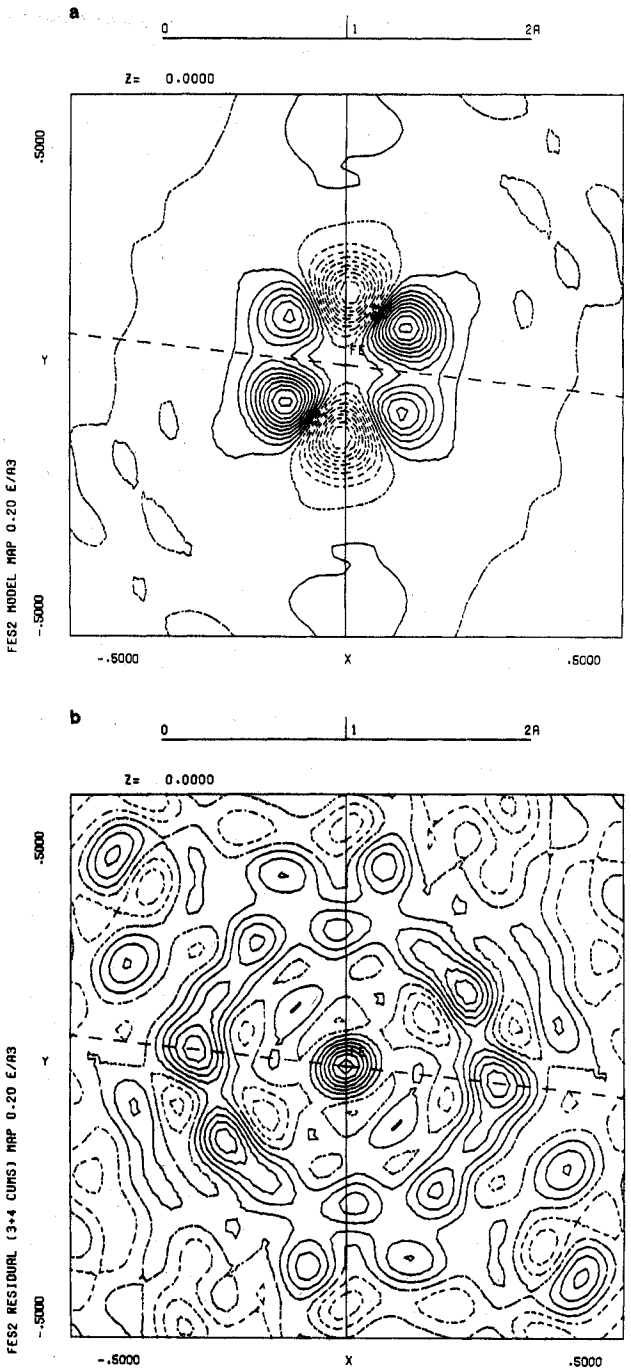

Figure 5. (a) Multipole model density and (b) residual density about the iron atom from parameters of refinement V. Both maps are calculated to a resolution of 1.46 Å^{-1} and include thermal smearing. Contours are plotted as in Figure 3a.

section is plotted in Figure 5b. The most significant feature of the residual density is a ring of excess density 0.8 Å from the iron atom. The inability of the model to fit this ring is attributed to the restricted form of the single Slater radial function used in the density fitting.

Discussion

The experimental electron density distribution around the iron atom is qualitatively similar to the distributions found in several other octahedral complexes.[2-4] Metal atoms with d-electron configurations that allow preferential occupation of the t_{2g} orbitals show peaks of excess charge density directed into the faces of the octahedron. A recent study of $K_2Na[Co(NO_2)_6]$ yields a density distribution about the transition-metal atom quite similar to that of pyrite with peaks of 1.69 (14) e/Å^3.[29] In the present study, the difference in peak heights also reveals an effect on the electron density from the distortion of the crystal field. Thus considerable information on the electronic structure is obtained by direct inspection of the experimental density.

However, since the d-electron density gives sharp features in the deformation maps, the peak heights are rather sensitive to the amount of thermal motion and resolution of the experiment. A large dependence on experimental resolution has

(29) S. Ohba, K. Toriumi, S. Sato, and Y. Saito, *Acta Crystallogr., Sect. B*, **34**, 3535 (1978).

been demonstrated for the t_{2g} peak heights of $K_2Na[Co(NO_2)_6]$.[29] The dependence of peak heights on the details of the particular experiment make them less satisfactory for obtaining quantitative information on the electronic structure.

Difficulties with the effects of resolution and thermal smearing are avoided by including multipole deformation functions in the least-squares model. In this study, quantitative information in the form of d-orbital occupancies has been obtained from the refined populations of the multipole functions, within the limitations of the crystal field approximation and minimal basis of Slater-type density functions. It is then necessary to consider whether these occupancies are compatible with the known diamagnetism of pyrite.

If the atomic wave function can be expressed by a single Slater determinant, integer values are expected for the occupation parameters P_1, P_2, and P_3 since each orbital can only be occupied by 0, 1, or 2 electrons. However, in the presence of a trigonally distorted octahedral crystal field, the e_g and e_g' orbitals belong to the same symmetry representation and may mix (Figure 1), giving new orbitals, $\varphi_{1\pm} = C_1(e_{g\pm}) + C_2(e_{g\pm}')$ and $\varphi_{2\pm} = C_2(e_{g\pm}) - C_2(e_{g\pm}')$, which are linear combinations of the original atomic basis set. Therefore, for any significant trigonal distortion from octahedral symmetry, the apparent occupancies of the e_g and e_g' orbitals, P_2 and P_3, may differ from integer values. Furthermore, noninteger orbital occupancies will result when more than one configuration contributes to the ground state of the atom in the crystal.

All of the d-orbital populations (Table V) derived from multipole refinements are significantly different from the values of 1.2, 2.4, and 2.4 for P_1, P_2, and P_3 expected for a spherical (high-spin) Fe(II) atom. Refinement V yields an occupancy of 2.00 (13) for the a_g orbital, in agreement with the value of 2.0 expected for low-spin Fe(II). The occupancies of the e_g and e_g' orbitals, $P_2 = 3.24$ (16) and $P_3 = 0.76$ (16), however, differ from the expected values of 4.0 and 0.0 corresponding to low-spin configuration in an octahedral field.

These populations may be understood in terms of the trigonal distortion that reduces the angles between ligands near the e_g orbitals, raising the energy of the e_g level (relative to the octahedral complex) by mixing with the e_g' orbitals. Occupancies of two electrons for the a_g orbital and four electrons for the $\varphi_{1\pm}$ orbitals could thus account for the values of P_2 and P_3 and also the observed diamagnetism of pyrite. However, the small value of P_4 seems to contradict this explanation.

Another possible explanation for the noninteger occupancies would be the presence of covalent overlap between the metal and ligand atoms. Though covalency effects are not evident in the density maps, the corresponding peaks may be too diffuse to be observed in this study. This possibility is supported by the long S–S distance (2.16 Å). If the 2.10-Å distance[30] found in SrS_2 is taken as the length of the S_2^{2-} ion, the longer bond found in pyrite suggests some covalent Fe–S interactions that destablize the S–S bond.

The refined ζ values of the iron atom are in a reasonable range for 3d electrons. The value of 3.77 (3) au^{-1} from refinement V corresponds to a slightly contracted d shell compared with the optimized single Slater exponent of 3.73 au^{-1} calculated for an isolated neutral iron atom.[31]

Conclusion

The distribution of d electrons in the low-spin Fe(II) atom of pyrite is directly revealed in the experimental electron density maps calculated from X-ray diffraction measurements. Pairing of the electrons in the presence of the strong crystal field results in a large observed asphericity of the electron density relative to a high-spin configuration. Further splitting of the t_{2g} orbitals by the trigonal distortion also produces an observable effect.

By fitting the data with density functions describing the atomic distortions, we obtain quantitative information on the occupancies of the iron d orbitals. The derived orbital occupancies have values that are quite reasonable for the crystal field in pyrite and are in agreement with the electric field gradient as derived from the Mössbauer quadrupole splitting.

The results described here for pyrite, as well as results from other charge density studies on systems containing transition metals, demonstrate the ability of X-ray measurements of the electron distribution to provide detailed information on the electronic structures of metal complexes. Further electron density studies may be expected to have a great impact on the understanding of more complicated systems such as metal-cluster compounds that cannot be described by simple theoretical models.

Acknowledgment. Support of this work by the National Science Foundation and by the donors of the Petroleum Research Fund, administered by the American Chemical Society, is gratefully acknowledged.

Registry No. Iron pyrite, 1309-36-0.

Supplementary Material Available: A listing of structure factor amplitudes (6 pages). Ordering information is given on any current masthead page.

(30) I. Kawada, K. Kato, and S. Yamaoka, *Acta Crystallogr., Sect. B*, **32**, 3110 (1976).
(31) E. Clementi and D. L. Raimondi, *J. Chem. Phys.*, **38**, 2686 (1963).